Journal of Materials Chemistry C

PAPER

View Article Online
View Journal | View Issue

Cite this: J. Mater. Chem. C, 2017, 5, 9488

Isomeric ligands enhance the anisotropy barrier within nine-coordinated {Dy_2} compounds†

Lin Sun,‡[a] Shilong Wei,‡[a] Jun Zhang,[b] Wenyuan Wang,[a] Sanping Chen,*[a] Yiquan Zhang,*[c] Qing Wei,[a] Gang Xie[a] and Shengli Gao[a]

Received 22nd June 2017,
Accepted 22nd August 2017

DOI: 10.1039/c7tc02786a

rsc.li/materials-c

Based on isomeric ligands, (2,4′-Hpcad = N^3-(2-pyridoyl)-4-pyridinecarboxamidrazone and 2,3′-Hpcad = N^3-(2-pyridoyl)-3-pyridinecarboxamidrazone), two carboxylate-bridged centrosymmetric Dy^{III} dimers, $[Dy_2(2,4'\text{-pcad})_2(C_2H_3O_2)_4(H_2O)_2]\cdot 4H_2O$ (**1**) and $[Dy_2(2,3'\text{-pcad})_2(C_2H_3O_2)_4(H_2O)_2]$ (**2**), were obtained, where Dy^{III} ions adopted a monocapped square antiprism coordination geometry, but exhibiting different distortions. Fine-tuning the structure on using isomeric ligands had a significant impact on the magnetic properties of compounds **1** and **2**. Magnetic studies revealed that **1** and **2** exhibit slow magnetic relaxation behaviours under a zero direct-current field exhibiting effective energy barriers (U_{eff}) of 53.5 K and 132.6 K, respectively, wherein compound **2** possesses the highest U_{eff} in nine-coordinated Dy_2 compounds. *Ab initio* calculations of compound **2** for magnetic interactions, magnetic axes inclination and charge distribution around Dy^{III} ions revealed simultaneous optimization of f–f interactions between the Dy^{III} ions and the stronger ligand field axis of individual Dy^{III} ion, which realizes excellent performance of **2**. These findings demonstrate an efficient approach to enhancing the magnetic anisotropy barrier on using isomeric ligands.

1 Introduction

Single-molecule magnets (SMMs) provide the fascinating possibility of creating switchable, molecular scale devices that store or manipulate information on orientating their molecular spin.[1–3] Their quantum coherent properties have sparked further interest in their potential applications, such as high-density data storage devices, spintronics and quantum computing.[4–8] In fact, lanthanides SMMs (Ln-SMMs) have been responsible for achieving the goal of high-performance SMMs due to the intrinsic large spin state and large magnetic anisotropy of some lanthanide ions (Dy^{III}, Tb^{III}, Ho^{III} and Er^{III}), pushing the frontiers to larger thermal energy barriers of magnetization reversal (U_{eff}) and higher blocking temperatures (T_B).[9–17]

Ln-Based monometallic SMMs or single-ion magnets (SIMs) have been widely investigated and reported in literature. Experimentally, a series of Dy^{III}-based SIMs displaying pentagonal bipyramidal coordination geometry (near D_{5h} local symmetry) have been synthesized,[14–17] which exhibit remarkable properties, such as higher effective energy barrier (U_{eff}) and blocking temperature (T_B) (1815 K[16] and 20 K,[17] respectively). Theoretically, *ab initio* calculations have provided a deeper interpretation of the relaxation dynamics of Dy^{III}-based SIMs.[18–22] In addition to the above-mentioned fascinating Ln-based SIMs, a few dinuclear lanthanide compounds also exhibit SMM properties,[23–37] representing the simplest molecular units which allow the study of magnetic interactions between two spin carriers. It has been reported that the SMM behaviours of lanthanide-based systems are extremely sensitive to the coordination geometry and ligand field effect coupled with the strength of magnetic interactions among the adjacent lanthanide sites. In dinuclear systems, the coordination environment could be modulated through a subtle change of the ligand field, including the effects of lattice solvents,[38,39] the coordinated solvents,[30] the pH values of the solution systems[40a] and the electrostatic environment.[27] On investigating such systems, one could expect to understand the nature and strength of interactions between lanthanide ions as well as possible alignment of spin vectors and anisotropy axes.[40b] Clearly, it remains a significant challenge to establish rational and effective guidelines for synthesizing Ln_2-SMMs, exploring the effect of f–f interactions and uniaxial anisotropy

[a] Key Laboratory of Synthetic and Natural Functional Molecule Chemistry of Ministry of Education, College of Chemistry and Materials Science, Northwest University, Xi'an, Shaanxi 710069, P. R. China. E-mail: sanpingchen@126.com
[b] School of Materials and Chemical Engineering, Anhui Jianzhu University, Hefei, 230601, China
[c] Jiangsu Key Laboratory for NSLSCS, School of Physical Science and Technology, Nanjing Normal University, Nanjing 210023, China. E-mail: zhangyiquan@njnu.edu.cn

† Electronic supplementary information (ESI) available: General experimental, synthesis and characterization of the compound mentioned in the manuscript, details of the single crystal diffraction experiments, XRPD, TG and additional figures. CCDC 1523394 (**1**) and 1469449 (**2**). For ESI and crystallographic data in CIF or other electronic format see DOI: 10.1039/c7tc02786a

‡ These authors have equal contribution to this study.

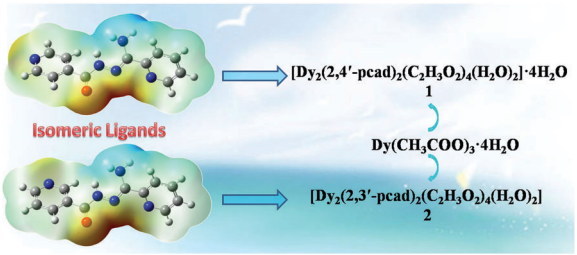

Scheme 1 Syntheses of compounds **1** and **2**.

on magnetic behaviour, and thereby obtaining magneto-structural correlations.

It is desirable to choose suitable organic ligands to achieve Ln_2-SMMs displaying defined geometry. In the present study, we select two isomeric tridentate Schiff-base ligands on the basis of Density Function Theory (DFT) calculations, N^3-(2-pyridoyl)-3-pyridinecarboxamidrazone (2,3′-Hpcad) and N^3-(2-pyridoyl)-4-pyridinecarboxamidrazone (2,4′-Hpcad). Herein, we successfully synthesized two symmetric dimer compounds displaying similar coordination geometry, $[Dy_2(2,4'\text{-pcad})_2(C_2H_3O_2)_4(H_2O)_2]\cdot 4H_2O$ (**1**) and $[Dy_2(2,3'\text{-pcad})_2(C_2H_3O_2)_4(H_2O)_2]$ (**2**) (Scheme 1). This study provides an example of fine-tuning coordination geometry through the use of isomeric ligands, then enhancing the anisotropy barrier in a Dy_2 system. Meanwhile, *ab initio* calculations were also performed to allow the determination of the principal magnetic axes, the strength of the magnetic interactions and the interpretation of the magnetic behaviour of the labelled compounds.

2 Experimental

2.1 Materials and instruments

All the materials and reagents were obtained commercially without further purification. The FT-IR spectra were recorded in the range of 400–4000 cm^{-1} using KBr pellets on an EQUINOX55 FT/IR spectrophotometer. Elemental analyses (C, H, N) were conducted on a Perkin-Elmer 2400 CHN elemental analyzer. The phase purity of polycrystalline samples was confirmed using powder X-ray diffraction (PXRD) measurements executed on a Rigaku RU200 diffractometer at 60 kV, 300 mA, and Cu Kα radiation (λ = 1.5406 Å), with a scan speed of 5° min^{-1} and a step size of 0.02° in 2θ. The simulated PXRD pattern was calculated using single-crystal X-ray diffraction data and processed using the Mercury 2.4[41] program provided by the Cambridge Crystallographic Data Center. Magnetic measurements were performed in the temperature range of 2–300 K with an applied field of 1000 Oe, using a Quantum Design MPMS-XL-7 SQUID magnetometer on the polycrystalline samples. The diamagnetic corrections for the compounds were estimated using Pascal's constants. Alternating current (ac) susceptibility experiments were performed using an oscillating ac field of 2.0 Oe at ac frequencies ranging from 1 to 1000 Hz. The magnetization was measured in the field range 0–7 T.

2.2 Synthesis of the compounds 1 and 2

2.2.1 Synthesis of $[Dy_2(2,4'\text{-pcad})_2(C_2H_3O_2)_4(H_2O)_2]\cdot 4H_2O$ (1). 2,4′-Hpcad was synthesized as described in the literature.[42] Solid $Dy(CH_3COO)_3\cdot 4H_2O$ (0.2 mmol, 0.082 g) was reacted with 2,4′-Hpcad (0.1 mmol, 0.024 g) in CH_3OH (15 mL) in the presence of triethylamine (0.2 mmol, 0.026 mL). The resultant yellow solution was further stirred for 6 h and then filtered. Pale yellow block-shaped crystals were gathered in one week with a yield of ~17% (based on Dy^{III} salt). Anal. calcd for $C_{32}H_{44}Dy_2N_{10}O_{16}$ (1149.77): C, 33.33; H, 3.85; N, 12.15. Found: C, 33.43; H, 3.86 N, 12.18. IR (KBr): 3482(b), 3104(w), 2989(w), 1643(s), 1588(w), 1460(m), 1403(m), 1278(w), 1205(m), 1149(m), 1104(w), 1046(w), 985(m), 889(m), 725(m), 659(w), 609(s), 528(m), 478 cm^{-1} (w).

2.2.2 Synthesis of $[Dy_2(2,3'\text{-pcad})_2(C_2H_3O_2)_4(H_2O)_2]$ (2). 2,3′-Hpcad was synthesized as described in the literature.[42] It was prepared in the same manner as compound **1**, except that 2,3′-Hpcad was used. Yellow needle-like crystals, suitable for X-ray analysis, were obtained with a yield of ~20% (based on Dy^{III} salts). Anal. calcd for $C_{32}H_{36}Dy_2N_{10}O_{12}$ (1077.71): C, 35.55; H, 3.36; N, 12.96. Found: C, 35.66; H, 3.37; N, 13.00. IR (KBr): 3420(b), 3065(w), 2941(w), 1634(s), 1554(w), 1460(m), 1370(m), 1271(w), 1205(m), 1139(m), 1093(w), 1043(w), 957(m), 903(m), 720(m), 656(w), 625(s), 543(m), 475 cm^{-1} (w).

2.3 DFT calculations

Based on theoretical research on the electronic configuration (ESI,† Fig. S1–S4 and Tables S1, S2), ligands 2,3′-Hpcad and 2,4′-Hpcad were designed and synthesized.

2.4 X-ray crystallography

The single crystal X-ray experiment was performed on a Bruker Apex II CCD diffractometer equipped with graphite-monochromatized Mo Kα radiation (λ = 0.71073 Å) using ω and φ scan mode. The data integration and reduction were processed with SAINT[43a] software. Absorption correction based on multi-scan was performed using the SADABS[43b] program. The structures were solved employing the direct method using SHELXTL[43c] and refined using full-matrix least-squares procedures on F^2 with the SHELXL-97[43d] and SHELXL-2014 programs.[43e] All non-hydrogen atoms were refined with anisotropic displacement parameters. Hydrogen atoms were located in their calculated positions and thereafter allowed to ride on their parent atoms. Experimental details associated with the crystal data, data collection parameters and refinement statistics are summarized in Table S3 (ESI†) while the selected bond lengths and angles are presented in Table S4 (ESI†).

2.5 Physical characterisation

The solvent (lattice and/or coordinated H_2O molecules) contents of **1** and **2** were determined on performing elemental (C, H, N) analysis and further confirmed on performing thermogravimetric analysis (TGA) under dry N_2 atmosphere (Fig. S5, ESI†). The mass loss values are consistent with $4H_2O$ (**1**) (it is highly possible that **1** would first lose two lattice water molecules due to the grinding before measurement) and $2H_2O$ (**2**) molecules per formula unit. In particular, the TGA curve of compound **1** shows the mass loss before 100 °C, corresponding to the loss of the lattice H_2O molecules. In order to confirm the phase purity

of the prepared samples of **1** and **2**, X-ray powder diffraction (XRPD) was carried out (Fig. S6, ESI†). The experimental patterns are consistent with the corresponding calculated ones, demonstrating the phase purity of **1** and **2**.

3 Results and discussion

3.1 Structure description

In the previous study,[34] $[Dy_2L_2(OAc)_4(MeOH)_2]\cdot 2MeOH$ (HL = (*E*)-*N*′(2-hydroxybenzylidene)-2-mercaptonicotinohydrazide) was prepared through slow volatilization of the solvent (CH_3OH–DMF (20 mL/2 mL) in the presence of triethylamine). Herein, we selected a similar method, but changed the solvent and the ratio of reactants. The labelled compounds were synthesized from $Dy(CH_3COO)_3\cdot 4H_2O$ and 2,4′-Hpcad/2,3′-Hpcad in a CH_3OH solution in the presence of triethylamine, with slow evaporation under ambient conditions (see synthesis of the compounds **1** and **2** for details).

Single-crystal X-ray diffraction analyses revealed that compounds **1** and **2** crystallize in the monoclinic space group (*C*2/*c* and $P2_1/n$, respectively). Their molecular structures are represented in Fig. 1. As shown in Fig. 1, all three compounds are centrosymmetric. The compounds **1** and **2** share a similar dinuclear structure, where each Dy^{III} is located in the chelating pocket formed due to the carboxyl-O, hydrazide-N and pyridine-N of the 2,4′-Hpcad and 2,3′-Hpcad, respectively (Fig. S7a and b, ESI†). The metal centers in compound **1** are bridged by the acetate groups (O17 and O6) in the form of $\eta^1{:}\eta^2{:}\mu_2$, with the Dy···Dy distance being 4.172(5) Å, the Dy1–O17^i–Dy1^i and Dy1–O6–Dy1^i angles being 65.21(1)° and 113.77(2)°, respectively. For compound **2**, the metal centers are bridged by the acetate groups (O1 and O4) in the form of $\eta^1{:}\eta^2{:}\mu_2$, with the Dy···Dy distance of 4.127(1) Å, the Dy1–O1–Dy1^i and Dy1–O4–Dy1^i angles being 65.15(2)° and 112.67(3)°, respectively. There are two coordination modes of the acetate groups in compounds **1** and **2**, as $\eta^1{:}\eta^2{:}\mu_2$ and η^2, which are shown in Fig. S7c and d. For **1** and **2**, Dy–O distances fall in the range of 2.306(9)–2.633(5) Å, and Dy–N distances fall in the range of 2.425(1)–2.573(3) Å. The Dy–O and Dy–N bond lengths in **1** are longer than those in compound **2** (Table S4, ESI†).

The coordination geometries of Dy ions in compounds **1** and **2** were calculated utilizing the SHAPE software 2.1.[44] As shown in Table S4 (ESI†), the calculation indicates that Dy^{III} centers in **1** and **2** are best described as a nine-coordinated spherical capped square-antiprismatic (C_{4v}) geometry, but with different distortions from the ideal geometry (Fig. S8 and Table S5, ESI†). The supramolecular architecture of compound **1** is formed through hydrogen-bonding interactions and π···π interactions with centroid-to-centroid distances of 3.48 Å and 3.83 Å, respectively (Fig. S9 and Table S6, ESI†). In the crystal packing, the structure of the dinuclear Dy_2 molecule in compound **2** is further strengthened through hydrogen-bonding interactions and π···π interactions with centroid-to-centroid distances of 3.67 Å (Fig. S10 and Table S7, ESI†). The shortest intermolecular Dy···Dy distance is 11.00 and 11.39 Å for **1** (Fig. S11, ESI†) and **2** (Fig. S12, ESI†), respectively.

3.2 Static (dc) magnetic properties

To probe the static magnetic behaviors, direct-current (dc) magnetic susceptibilities in an applied field of 1000 Oe were measured on the polycrystalline samples of **1** and **2** over a temperature range of 2–300 K (Fig. 2). The $\chi_M T$ values at 300 K are 27.95 and 28.71 cm^3 K mol^{-1} for **1** and **2**, respectively, which are in agreement with the expected value of 28.34 cm^3 K mol^{-1} for two uncoupled Dy^{III} ions in the $^6H_{15/2}$ ground state (S = 5/2, L = 5, g = 4/3). The $\chi_M T$ values remain broadly constant from 300 K to 110 K, following the first drop as the temperature decreases further. Below approximately 15 K, we observed a second rapid drop in $\chi_M T$ for **1** and **2** decreasing to reach a minimum of 18.07 cm^3 K mol^{-1} and 17.49 cm^3 K mol^{-1} at about 2 K, respectively. The sharp decline of the $\chi_M T$ values at low temperatures may be attributed to three possible reasons:

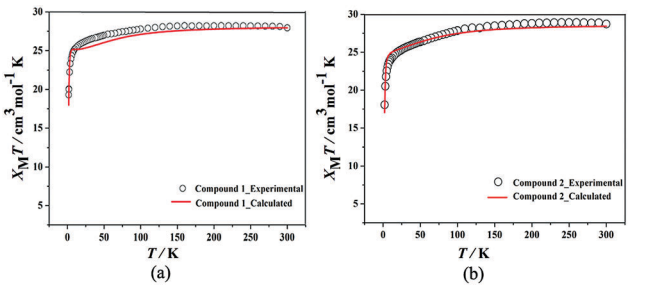

Fig. 2 $\chi_M T$ *versus* T plots for **1** (a) and **2** (b) at 1000 Oe. The solid lines show the calculated curves.

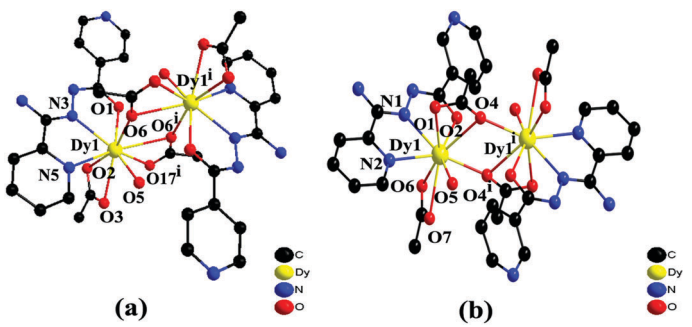

Fig. 1 Molecular structures of **1** (a) and **2** (b). The H atoms are omitted for clarity (**1**: $^i -x + 1/2, -y + 3/2, -z + 1$; **2**: $^i 1 - x, 1 - y, 1 - z$).

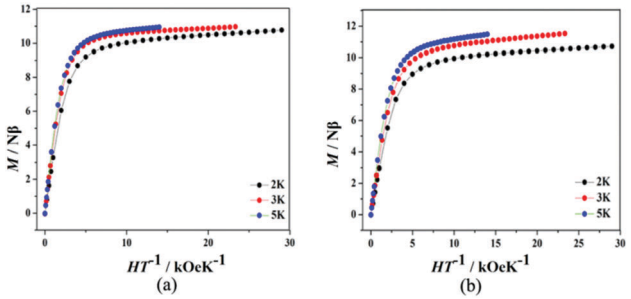

Fig. 3 Experimental *M versus* HT^{-1} plots of **1** (a) and **2** (b) at different temperatures.

antiferromagnetic coupling, thermal depopulation of low lying crystal field states and magnetic anisotropy.[45]

Magnetization (M) data for **1** and **2** were collected at 2, 3 and 5 K in the field range of 0–7 T (Fig. 3). The magnetization increases smoothly with increasing applied dc field without complete saturation even at 7 T. The magnetization values of **1** (10.95 Nβ) and **2** (10.90 Nβ) at 7 T are lower than the theoretical saturated value of 20 Nβ anticipated for two independent Dy^{III} ions, which could be attributed to the ligand-field-induced splitting of the Stark level as well as magnetic anisotropy.[46] Furthermore, the magnetization *versus* H/T plots at different temperatures show non-superimposed magnetization curves for compounds **1** and **2**, suggesting the magnetic anisotropy and/or low-lying excited states.

3.3 Dynamic (ac) magnetic properties

In order to reveal the dynamic magnetic behaviours of **1** and **2**, the temperature dependencies of the alternating current (ac) susceptibility were measured under a zero dc field with an ac field of 2.0 Oe (Fig. S13 and S14, ESI†). For **1**, the peaks in the imaginary part χ_M'' begin to emerge as the peak temperature decreases from 12.0 to 5.4 K in accordance with a reduction in the frequency from 1000 to 10 Hz (Fig. S13b, ESI†). For **2**, the peaks of χ_M'' could be clearly observed between 5.5 K (1 Hz) and 15.5 K (1000 Hz) (Fig. S14b, ESI†). Compounds **1** and **2** showed strong frequency dependent in-phase (χ_M') and out-of-phase (χ_M'') signals along with good peak shapes, revealing the typical slow magnetic relaxation behaviours of SMMs.

Furthermore, the dynamics of the magnetization of **1** and **2** have been studied by measuring their frequency dependencies on the ac susceptibility under a zero dc field. As shown in Fig. 4 and 5, both χ_M' and χ_M'' signals of **1** and **2** exhibit temperature dependencies, suggesting the presence of slow magnetic relaxation. The relaxation times (τ) extracted from the χ'' peaks for **1** and **2** at selected temperatures were used to construct the Arrhenius plot shown in Fig. S19 (ESI†). For **1** and **2**, $\ln(\tau)$ *vs.* T^{-1} plots were fitted to provide effective energy barriers (U_{eff}) of 48.9 K and 100.7 K with pre-exponential factors (τ_0) of 7.4×10^{-6} and 3.9×10^{-7} s, respectively. It is worth noting that the strong linear dependence of $\ln(\tau)$ at the high temperature region is indicative of a dominant Orbach relaxation mechanism, whilst at the low temperature region its curvature suggests the presence of other possible

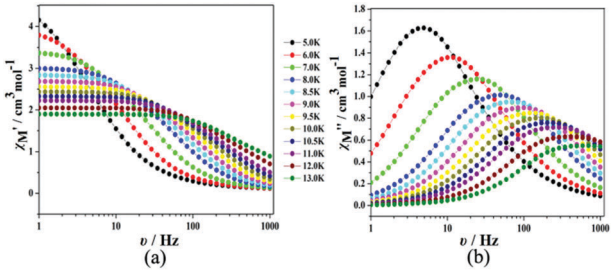

Fig. 4 Frequency dependence of the in-phase (a) and out-of phase (b) ac susceptibility signals under a zero dc field for **1**.

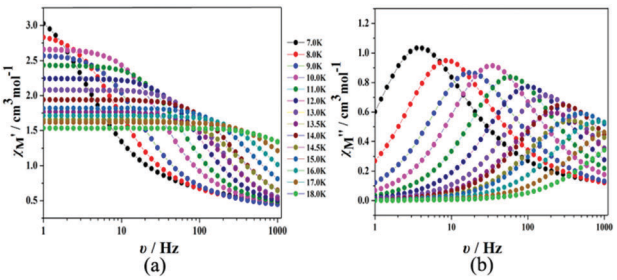

Fig. 5 Frequency dependence of the in-phase (a) and out-of phase (b) ac susceptibility signals under a zero dc field for **2**.

relaxation pathways.[47] A temperature independent regime was not observed, indicating that the competing relaxation process could not be QTM. Therefore, the relaxation occurs *via* the temperature dependent Orbach and Raman mechanisms (Fig. 6). Fitting the three data sets with eqn (1) yields $U_{eff}^{(1)}$ = 53.5 K (37.2 cm^{-1}), $\tau_0^{(1)} = 5.7 \times 10^{-6}$ s, $C^{(1)} = 0.36\ s^{-1}\ K^{-n}$, $n^{(1)}$ = 2.6; $U_{eff}^{(2)}$ = 132.6 K (92.2 cm^{-1}), $\tau_0^{(2)} = 3.8 \times 10^{-7}$ s, $C^{(2)} = 3.6 \times 10^{-3}\ s^{-1}\ K^{-n}$, n = 5.8, respectively.

$$\tau^{-1} = CT^n + {\tau_0}^{-1} \exp(-U_{eff}/kT). \quad (1)$$

The Cole–Cole plots (χ_M'' *vs.* χ_M') for **1** and **2** based on frequency-dependent ac susceptibility data present semi-circular shapes (Fig. 7). On fitting the corresponding data with a generalized Debye model,[48] the parameter (α) could be obtained in the range of 0.24–0.10 and 0.22–0.03 for **1** and **2**, respectively (Tables S8 and S9, ESI†), indicating a narrow distribution of relaxation times for a single relaxation process.

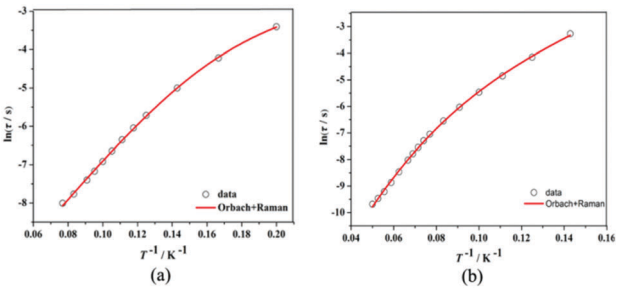

Fig. 6 Magnetization relaxation time ($\ln(\tau)$) *versus* T^{-1} plots under a zero dc field for **1** (a) and **2** (b). The solid red line represents the best fitting to the multiple relaxation process (eqn (1), see text for parameters).

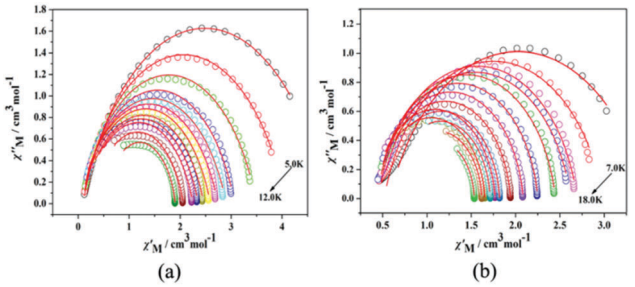

Fig. 7 The Cole–Cole plots of **1** (a) and **2** (b) with red solid lines as Debye fits.

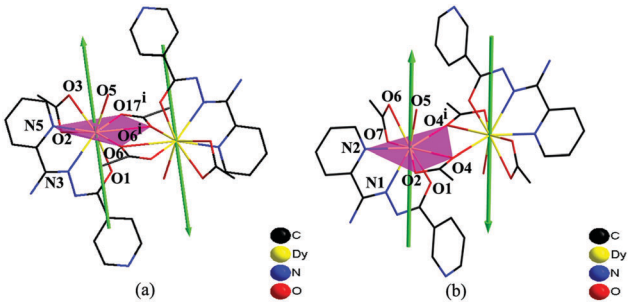

Fig. 8 Orientations of the local main magnetic axes of the ground doublets on Dy^{III} ions of **1** (a) and **2** (b).

3.4 Theoretical investigation

To gain further insight into the magnetization reversal in these compounds, *ab initio* calculations were performed. Complete-active-space self-consistent field (CASSCF) calculations on one type of individual Dy^{III} fragment for each of the compounds **1** and **2** on the basis of X-ray crystallography determined geometries have been carried out using MOLCAS 8.0[49] and SINGLE_ANISO[50–52] programs (see ESI† for details). The lowest spin–orbit energies and the corresponding g tensors of compounds **1** and **2** are shown in Table S10 (ESI†). The calculated ground g_z values of the Dy^{III} fragments are 19.617 and 19.581 for compounds **1** and **2**, respectively, which shows that the Dy^{III}–Dy^{III} interactions in compounds **1** and **2** could be approximately regarded as the Ising type. The program POLY_ANISO[50–52] (Fig. 2) was used to fit the magnetic susceptibilities of compounds **1** and **2** using the exchange parameters from Table 1. All parameters from Table S10 (ESI†) were calculated with respect to the pseudospin $\hat{S} = 1/2$ of the Dy^{III} ions. The total coupling parameter (J, dipolar and exchange) was included to fit the magnetic susceptibilities. The calculated and experimental $\chi_M T$ *versus* T plots of compounds **1** and **2** are shown in Fig. 2, where the fits are close to the experimental data.[53] From Table 1, the Dy^{III}–Dy^{III} interactions calculated for the two compounds using Lines model[54] are all antiferromagnetic. The main magnetic axes on the Dy^{III} ions for the two compounds are indicated in Fig. 8, where the magnetic axes on Dy^{III} for each compound are antiparallel to each other because of the Dy^{III}–Dy^{III} antiferromagnetic interaction. In addition, we summarized the exchange energies and the main values of the g_z for the lowest two exchange doublets of the two compounds (Table S11, ESI†), where the g_z values of the ground exchange states for all the complexes are close to 0, which confirms that the Dy^{III}–Dy^{III} couplings are all antiferromagnetic. As mentioned above, the evident antiferromagnetic interaction between Dy^{III} ions is likely related to the relatively small Dy–O–Dy angles within the dinuclear core and/or the small dihedral angle between the Dy_2O_2 plane and the benzene ring.[55,56]

According to the orientation of the magnetic easy axis (g_z) of **1**, obtained from the *ab initio* results (Fig. 8), the ligand atoms of the first sphere could be categorized into two groups: (1) equatorial atoms consisting of the four oxygen atoms (O2, O6, $O6^i$ and $O17^i$) and one nitrogen atom (N5) from the pyridine ring that compose the equatorial plane; (2) axial atoms consisting of one nitrogen atom (N3) of the ligand and the three oxygen atoms (O1, O3 and O5) that lie along the axial direction. We observed that the average charge (−0.656) of the proximate pentagonal plane was lower than that (−0.675) of the magnetic axes in compound **1**, which resulted in a stronger easy-axis ligand field corresponding with the smaller g_x and g_y values for the ground states. Similar categorization of the atoms of the first coordination sphere is also observed in **2**, in which four oxygen atoms and one nitrogen atom form the equatorial plane and one nitrogen atom and three oxygen atoms lie along the axial direction (Fig. 7b). The magnetic easy axis lies close to the shorter Dy–O bond, approximating to O1 and O2 atoms in **2**. It is worth noting that O1 atom (−0.843) and O2 atom (−0.766), with higher negative charge values, are the shorter coordination bonds in this molecule (Table S12, ESI†), resulting in the stronger coordination affinity. The average charges on the proximate pentagonal plane (−0.656) are lower than those of the axial coordination atoms (−0.678) in compound **2**, giving rise to the stable maximum $|J_z|$ value of 15/2 for the ground state sublevel due to the lowering of the electron repulsion for the proximate pentagonal plane, thus causing easy axial anisotropic ground states, which is in agreement with the negligible g_x and g_y values for the ground states. Therefore, the charge density distribution surrounding the magnetic Dy^{III} centers is considered as an important factor in modulating the entire molecular magnetic anisotropy in the Dy_2 system.

The calculated energy gaps between the ground and the first excited KD for the individual Dy^{III} fragments of **1** and **2** are 104.4 and 121.9 cm^{-1}, respectively. For compound **1**, the corresponding U_{eff} value of 37.2 cm^{-1} is far lower than the theoretical value. The calculated U_{eff} value of 121.9 cm^{-1} from the *ab initio* calculations is higher than the experimentally determined U_{eff} value (92.2 cm^{-1}) for compound **2**. The origin of this deviation between experiments and calculations is probably related to the existence of extra relaxation behaviours

Table 1 Fitted exchange coupling constants, J_{exch}, the calculated dipole–dipole interactions, $J_{dipolar}$ and the total J between Dy^{III} ions in **1** and **2** (cm^{-1}). The intermolecular interactions (zJ') of **1** and **2** are all fit to 0.08 cm^{-1}

	1	**2**
$J_{dipolar}$	−2.10	−2.09
J_{exch}	−1.00	−1.25
J	−3.10	−3.34

(competitive processes such as Raman, direct and quantum tunnelling).[57]

3.5 Magneto-structural correlations

The structural comparison of the coordination spheres in compounds **1** and **2** is required to understand the origin of the magnetization dynamics. As seen from Fig. 1, compound **1** has the N_2O_7 coordination environment generated using three atoms from 2,4′-pcad$^-$ (O1, N3 and N5), two O atoms (O2 and O3) from CH_3COO^-, three O atoms (O17^i, O6 and O6^i) from bridged CH_3COO^- and one O atom (O5) from H_2O molecules. Compared with **1**, compound **2** exhibits the N_2O_7 coordination environment with different distortions from the ideal geometry, attributed to the minor distinction in the location of pyridine-N atoms from the isomeric ligands (2,3′-Hpcad and 2,4′-Hpcad). Even tiny change of ligand generating the slight adjustment of coordination geometry drastically influences the overall magnetic properties of the molecule. Based on *ab initio* calculations, we observe compounds **1** and **2** have something in common: (1) the magnetic axes on Dy^{III} for each compound are antiparallel; (2) the Dy^{III}–Dy^{III} interactions in two compounds within Lines model are all antiferromagnetic; (3) the calculated ground g_z values of individual Dy^{III} fragment are 19.617 and 19.581 for compounds **1** and **2**. Certainly, there are a few differences: (1) the differences between the calculated energy gaps for the individual Dy^{III} fragments of **1** and the experimental U_{eff} value are higher than those of **2**, which indicate that a Raman process could account for the entire relaxation behaviour of compound **1**. (2) On basis of charge analysis, the same average charges of the proximate pentagonal plane in compounds **1** and **2**, as well as the higher average charges of axial coordination atoms in compound **2**, indicate that compound **2** exhibits stronger axial coordination filed. For the Dy_2 system, exchange coupling plays a critical role in modulating the magnetic behaviours. The values of the total coupling interactions for compounds **1** and **2** are approximate, but the value of **2** (J_{total}) is slightly greater than that of **1**. As illustrated in Fig. 8, the easy axis of **1** and **2** is not parallel to the vector connecting the two Dy^{III}, resulting in transversal components of the dipolar field induced by the dysprosium ions on each other, thus significantly increasing

Table 2 Configuration parameters and relaxation parameters with nine-coordinated Dy_2 compounds

Molecular formula (dimension)	Coordination number/configuration/CShM's values[a]	Bond distance/Å		The slow relaxation process			
		Dy···Dy$_{inter}$	Dy···Dy$_{intra}$	DC field/Oe	τ_0/s	U_{eff}/K	Ref.
$[Dy_2(2,4'\text{-pcad})_2(C_2H_3O_2)_4(H_2O)_2]\cdot 4H_2O$ (**1**)	9/CSAPR-9/2.336	11.00	4.17	0	5.7×10^{-6}	53.5	In this study
$[Dy_2(2,3'\text{-pcad})_2(C_2H_3O_2)_4(H_2O)_2]$ (**2**)	9/CSAPR-9/2.167	11.39	4.13	0	3.8×10^{-7}	132.6	
$[Dy_2(DMOP)_2(NTFA)_4(CH_3OH)_2\cdot 2H_2O]$ (**3**)	9/TCTPR-9/1.164	9.66	3.94	0	1.2×10^{-6}	56.2	23
				1500	7.9×10^{-7}	58.8	
$[Dy_2(NO_3)_4(sacbH)_2(H_2O)_2(MeCN)_2]$ (**4**)	9/TCTPR-9/1.650	8.54	5.10	0	1.4×10^{-7}	109.3	24
				1000	1.1×10^{-7}	128.2	
					2.7×10^{-5}	62.3	
$[Dy(L_1)_3(DMSO)(H_2O)]_2$ (**5**)	9/CSAPR-9/2.296	9.53	4.16	2000	—	—	25
$\{[Dy_2(PDOA)_3(H_2O)_6]\cdot 2H_2O\}_n$ (**6**)	9/CSAPR-9/1.742	6.41	13.92	2000	6.3×10^{-10}	71.6	26
$[Dy_2(PDOA)_3(H_2O)_6]\cdot 3.5H_2O$ (**7**)	9/CSAPR-9/1.186	6.13	12.39	2000	2.4×10^{-11}	97.8	
$[Dy_2(\mu_2\text{-anthc})_4(anthc)_2(2,2'\text{-bpy})_2]$ (**8**)	9/CSAPR-9/2.300	9.32	3.95	0	3.2×10^{-8}	51.2	27
$[Dy_2(\mu_2\text{-anthc})_4(anthc)_2(1,10\text{-phen})_2]$ (**9**)	9/CSAPR-9/1.740	9.80	3.92	0	4.6×10^{-9}	49.4	
$[Dy_2(\mu_2\text{-anthc})_4(anthc)_2L_2]$ (**10**)	9/CSAPR-9/1.878	11.75	3.92	0	3.4×10^{-8}	31.6	
$[Dy_2(HL_1)_2(NO_3)_4]$ (**11**)	9/CSAPR-9/2.948	3.71	7.04	No peaks	—	—	28
$[Dy_2(L_2)_2(NO_3)_4]$ (**12**)	9/TCTPR-9/2.048	3.71	8.42	1000	8.5×10^{-8}	72.48	
$[Dy_2(HL_3)_2(NO_3)_4]$ (**13**)	9/TCTPR-9/2.018	3.72	9.00	0	8.5×10^{-7}	41.55	
				2000	1.2×10^{-7}	72.37	
$[Dy_2(H_2L)_2(\mu\text{-piv})_2(piv)_2]\cdot 2CHCl_3$ (**14**)	9/CSAPR-9/0.968	3.63	—	0	8.81×10^{-5}	8.96	29
				0	1.48×10^{-6}	35.5	
$[Dy_2(ovph)_2Cl_2(H_2O)_3(EtOH)]$ (**15**)	9/CSAPR-9/1.221 7/PBPY-7/1.410	3.95	6.26	0	1.4×10^{-7}	110	30
$[Dy_2(H_3L)_2(PhCOO)_4]\cdot 4H_2O$ (**16**)	9/CSAPR-9/1.408	3.69	>7.6	0	1.3×10^{-7}	42.7	31
$[Dy(H_2L^1)_2(NO_3)_3]_2\cdot 2CH_2Cl_2\cdot 2CH_3OH$ (**17**)	9/CSAPR-9/2.873	—	9.37	2000	3.0×10^{-6}	43.0	32
$[Dy_2(bzhdep\text{-}2H)(NO_3)_4(DMF)_4]$ (**18**)	9/CSAPR-9/2.319	—	7.88	1000	2.6×10^{-6}	29.5	33
$[Dy_2L_2(OAc)_4(MeOH)_2]\cdot 2MeOH$ (**19**)	9/CSAPR-9/1.197	—	4.07	0	6.4×10^{-7}	39.1	34
$[Dy_2(Mq)_4(NO_3)_6]$ (**20**)	9/CSAPR-9/2.401	9.60	3.91	0	5.4×10^{-6}	40.01	35
$[Dy_2L(H_2L)(teaH_2)(o\text{-vanillin})(H_2O)]\text{-}(ClO_4)_2\cdot 2CH_3OH\cdot H_2O$ (**21**)	9/CSAPR-9/1.283 9/CSAPR-9/1.154	—	3.55	0	1.7×10^{-4}	1.4	36
$[Dy_2(hfac)_6(H_2O)_4pz]\cdot 2pz$ (**22**)	9/TCTPR-9/0.530	6.41	8.09	0	8.4×10^{-10}	110.8	37

[a] CShM's values of the Dy^{III} ion in comparison with all of the reference standard *n*-coordinate polyhedrons were calculated using the SHAPE 2.1 program.[23] 2,6-Dimethoxyphen (DMOP), 2-naphtoyltrifluoroacetone (NTFA), benzoyltrifluoroacetone (BTFA), thenoyltrifluoroaceton (TTA);[24] *N*-salicylidene-2-amino-5-chlorobenzoic acid ($sacbH_2$);[25] 2-methoxycinnamic acid (L1);[26] 1,2-phenylenedioxydiacetic acid (H_2PDOA);[27] 2,2′-bipyridyl (2,2′-bpy), 1,10-phenanthroline (1,10-phen), 4,7- dimethyl-1,10′-phenanthroline (L), 9-anthracenecarboxylate (anthc$^-$);[28] 2-[(2-hydroxyethyl)-pyridin-2-ylmethylamino]-ethanol (H_2L_1), 2-(bis-pyridin-2-ylmethylamino)-ethanol (HL_2), 2-(bis-pyridin-2-ylmethylamino)-propane-1,3-diol (H_2L_3);[29] 2,2′-(2-hydroxy-3-methoxy-5-methylbenzylazanediyl)diethanol (H_3L);[30] pyridine-2-carboxylic acid [(2-hydroxy-3-methoxyphenyl)methylene] hydrazide (H_2ovph);[31] 1,5-bis(2-hydroxy-3-methoxybenzylidene)carbonohydrazide (H_4L);[32] *N*,*N*′-(1,3-propylene)bis(salicylideneimine) (H_2L^1);[33] pyrazine-2,5-diylbis(ethan-1-yl-1-ylidene)di(benzohydrazide) (bzhdep);[34] (*E*)-*N*′-(2-hydroxybenzylidene)-2-mercaptonicotinohydrazide (HL);[35] 8-hydroxy-2-methylquinoline (Mq);[36] triethanolamine ($teaH_3$); *N*,*N*-bis(3-methoxysalicylidene)-1,2-cyclohexanediamine (H_2L);[37] hexafluoroacetylacetonate (hfac), pyrazine (pz).

the efficiency of the tunnelling mechanism. Therefore, the calculated U_{eff} value is larger than the experimentally determined U_{eff} value for compound **2**, on account that relaxation of the magnetization occurs *via* the lower lying excited states and competitive processes such as Raman and direct ones, rather than from a multistep Orbach process above the ladder. However, moderate f–f interactions[58] could suppress QTM under a zero dc field, hence realizing the corresponding U_{eff} value close to the theoretical value (between the ground and the first excited KD).

In our previous study[59] based on three mononuclear nine-coordination Dy^{III} compounds, *ab initio* calculations revealed that the Kramers doublet ground state is predominantly axial with the g_z tensors of three compounds (19.519, 19.535 and 19.337), matching the Ising-limit factor of 20 anticipated for the pure $M_J = \pm 15/2$ state, whereas they exhibit filed-induced slow magnetic relaxation behaviours. In this study, compounds **1** and **2** with the approximate g_z values, exhibit SMM behaviours under a zero dc field, further confirming that moderate f–f interactions are vital to obtain a SMM with excellent performances.

To explore the relationship between configuration and magnetic relaxation behaviours, configuration parameters and relaxation parameters of nine-coordinated Dy_2 SMMs are summarized in Table 2.[23–37] The configurations of compounds **1–21** are all C_{4v}-CSAPR or D_{3h}-TCTPR, exhibiting slow magnetic relaxation under a zero/non-zero dc field. Notably, this configuration is closer to a single configuration (C_{4v}-CSAPR or D_{3h}-TCTPR), but not always showing better SMM behaviours. Consequently, neither C_{4v}-CSAPR nor D_{3h}-TCTPR is the most ideal geometry exhibiting high axiality. The magnetic axis and the axis of symmetry try to overlap in one direction; for example, five atoms form the equatorial plane with four atoms of symmetry lie up and down with respect to the plane. In terms of theoretical calculations of the magnetic easy axis and charge distribution of the coordinated atoms, compound **2** exhibiting the stronger axis coordination field displays remarkable SMM performance with the highest U_{eff} (132.6 K) in nine-coordinated Dy_2 compounds. In brief, the simultaneous optimization of f–f interactions between the magnetic ions (to suppress quantum tunnelling) and the axis coordination field (to generate high anisotropy barriers) are mandatory in order to produce excellent performance in Dy_2 SMMs.

4 Conclusions

In summary, both dinuclear Dy^{III} compounds **1** and **2** exhibiting the SMM behaviours under a zero dc field have been synthesized using isomeric ligands (2,3′-Hpcad and 2,4′-Hpcad) to realize ligand filed fine-tuning. Although **1** and **2** have the same nine-coordinate monocapped square antiprism coordination geometry around each Dy^{III} ion, they present different distortions from the ideal geometry. Magnetic analyses show that **1** and **2** exhibit slow magnetic relaxation behaviours under a zero dc field. For compound **1**, the corresponding U_{eff} value of 53.5 K is far lower than the theoretical value, indicating that a Raman process could account for the entire relaxation behaviour except for quantum tunnelling. Compound **2** possesses the highest U_{eff} (132.6 K) in nine-coordinated Dy_2 compounds, ascribed to simultaneous optimization of f–f interactions between the magnetic ions and of the stronger axis coordination filed. These findings demonstrate an efficient approach to enhancing the magnetic anisotropy barrier using isomeric ligands. Notably, this strategy in combination with the guidance of DFT calculations to design isomeric ligands, experimental observations and the interpretation of *ab initio* calculations provide an in-depth understanding of the f–f interactions between the magnetic ions and uniaxial anisotropy of individual magnetic ions in the Ln_2 system.

Conflicts of interest

There are no conflicts to declare.

Acknowledgements

We gratefully acknowledge financial support from the National Natural Science Foundation of China (grant no. 21373162, 21673180, 21727805, 21673181, 21605121, 21671003 and 21473135) and Natural Science Foundation of Jiangsu Province of China (BK20151542).

References

1 A. R. Rocha, V. M. García-Suárez, S. W. Bailey, C. J. Lambert, J. Ferrer and S. Sanvito, *Nat. Mater.*, 2005, **4**, 335–339.
2 L. Bogani and W. Wernsdorfer, *Nat. Mater.*, 2008, **7**, 179–186.
3 M. Affronte, *J. Mater. Chem.*, 2009, **19**, 1731–1737.
4 D. Gatteschi, R. Sessoli and J. Villain, *Molecular nanomagnets*, Oxford University Press, Oxford, 2006.
5 M. Mannini, F. Pineider, P. Sainctavit, C. Danieli, E. Otero, C. Sciancalepore, A. M. Talarico, M. A. Arrio, A. Cornia, D. Gatteschi and R. Sessoli, *Nat. Mater.*, 2009, **8**, 194–197.
6 M. N. Leuenberger and D. Loss, *Nature*, 2001, **410**, 789–793.
7 J. Lehmann, A. Gaita-Arino, E. Coronado and D. Loss, *Nat. Nanotechnol.*, 2007, **2**, 312–317.
8 M. Ganzhorn, S. Klyatskaya, M. Ruben and W. Wernsdorfer, *Nat. Nanotechnol.*, 2013, **8**, 165–167.
9 S. Osa, T. Kido, N. Matsumoto, N. Re, A. Pochaba and J. Mrozinski, *J. Am. Chem. Soc.*, 2004, **126**, 420–421.
10 N. Ishikawa, M. Sugita, T. Ishikawa, S. Y. Koshihara and Y. Kaizu, *J. Am. Chem. Soc.*, 2003, **125**, 8694–8695.
11 D. N. Woodruff, R. E. P. Winpenny and R. A. Layfield, *Chem. Rev.*, 2013, **113**, 5110–5148.
12 R. J. Blagg, L. Ungur, F. Tuna, J. Speak, P. Comar, D. Collison, W. Wernsdorfer, E. J. L. McInnes, L. F. Chibotaru and R. E. P. Winpenny, *Nat. Chem.*, 2013, **5**, 673–678.
13 S. D. Jiang, B. W. Wang, H. L. Sun, Z. M. Wang and S. Gao, *J. Am. Chem. Soc.*, 2011, **133**, 4730–4733.
14 S. K. Gupta, T. Rajeshkumar, G. Rajaraman and R. Murugavel, *Chem. Sci.*, 2016, **7**, 5181–5191.
15 J. Liu, Y. C. Chen, J. L. Liu, V. Vieru, L. Ungur, J. H. Jia, L. F. Chibotaru, Y. Lan, W. Wernsdorfer, S. Gao, X. M. Chen and M. L. Tong, *J. Am. Chem. Soc.*, 2016, **138**, 5441–5450.

16 Y. S. Ding, N. F. Chilton, R. E. P. Winpenny and Y. Z. Zheng, *Angew. Chem., Int. Ed.*, 2016, **55**, 16071–16074.
17 Y. C. Chen, J. L. Liu, L. Ungur, J. Liu, Q. W. Li, L. F. Wang, Z. P. Ni, L. F. Chibotaru, X. M. Chen and M. L. Tong, *J. Am. Chem. Soc.*, 2016, **138**, 2829–2837.
18 J. D. Rinehart and J. R. Long, *Chem. Sci.*, 2011, **2**, 2078–2085.
19 L. Ungur and L. F. Chibotaru, *Phys. Chem. Chem. Phys.*, 2011, **13**, 20086–20090.
20 Nicholas F. Chilton, Conrad A. P. Goodwin, David P. Mills and Richard E. P. Winpenny, *Chem. Commun.*, 2015, **51**, 101–103.
21 Nicholas F. Chilton, *Inorg. Chem.*, 2015, **54**, 2097–2099.
22 L. Ungur and L. F. Chibotaru, *Inorg. Chem.*, 2016, **55**, 10043–10056.
23 H. R. Tu, W. B. Sun, H. F. Li, P. Chen, Y. M. Tian, W. Y. Zhang, Y. Q. Zhang and P. F. Yan, *Inorg. Chem. Front.*, 2017, **4**, 499–508.
24 E. C. Mazarakioti, J. Regier, L. Cunha-Silva, W. Wernsdorfer, M. Pilkington, J. Tang and T. C. Stamatatos, *Inorg. Chem.*, 2017, **56**, 3568–3578.
25 O. Khalfaoui, A. Beghidja, J. Long, A. Boussadia, C. Beghidja, Y. Guari and J. Larionova, *Dalton Trans.*, 2017, **46**, 3943–3952.
26 R. Boča, M. Stolárová, L. R. Falvello, M. Tomás, J. Titiša and J. Černák, *Dalton Trans.*, 2017, **46**, 5344–5351.
27 Y. L. Wang, C. B. Han, Y. Q. Zhang, Q. Y. Liu, C. M. Liu and S. G. Yin, *Inorg. Chem.*, 2016, **55**, 5578–5584.
28 Y. Peng, V. Mereacre, A. Baniodeh, Y. H. Lan, M. Schlageter, G. E. Kostakis and A. K. Powell, *Inorg. Chem.*, 2016, **55**, 68–74.
29 P. Bag, C. K. Rastogi, S. Biswas, S. Sivakumar, V. Mereacre and V. Chandrasekhar, *Dalton Trans.*, 2015, **44**, 4328–4340.
30 Y. Jiang, G. Brunet, R. J. Holmberg, F. Habib, I. Korobkov and M. Murugesu, *Dalton Trans.*, 2016, **45**, 16709–16715.
31 H. S. Ke, S. Zhang, X. Li, Q. Wei, G. Xie, W. Y. Wang and S. P. Chen, *Dalton Trans.*, 2015, **44**, 21025–21031.
32 X. Y. Zou, P. F. Yan, Y. P. Dong, F. Luan and G. M. Li, *RSC Adv.*, 2015, **5**, 96573–96579.
33 W. Huang, F. X. Shen, S. Q. Wu, L. Liu, D. Y. Wu, Z. Zheng, J. Xu, M. Zhang, X. C. Huang, J. Jiang, F. F. Pan, Y. Li, K. Zhu and O. Sato, *Inorg. Chem.*, 2016, **55**, 5476–5484.
34 H. X. Zhang, S. Y. Lin, S. F. Xue, C. Wang and J. Tang, *Dalton Trans.*, 2014, **43**, 6262–6268.
35 F. Yang, Q. Zhou, G. Zeng, G. H. Li, L. Gao, Z. Shi and S. H. Feng, *Dalton Trans.*, 2014, **43**, 1238–1245.
36 L. Zhang, P. Zhang, L. Zhao, S. Y. Lin, S. F. Xue, J. Tang and Z. L. Liu, *Eur. J. Inorg. Chem.*, 2013, 1351–1357.
37 Y. Ma, G. F. Xu, X. L. Yang, C. Li, J. Tang, S. P. Yan, P. Cheng and D. Z. Liao, *Chem. Commun.*, 2010, **46**, 8264–8866.
38 X. J. Zhang, V. Vieru, X. W. Feng, J. L. Liu, Z. J. Zhang, B. Na, W. Shi, B. W. Wang, A. K. Powell, L. F. Chibotaru, S. Gao, P. Cheng and J. R. Long, *Angew. Chem., Int. Ed.*, 2015, **54**, 9861–9865.
39 W. B. Sun, B. Yan, L. H. Jia, B. W. Wang, Q. Yang, X. Cheng, H. F. Li, P. Chen, Z. M. Wang and S. Gao, *Dalton Trans.*, 2016, **45**, 8790–8794.
40 (*a*) L. N. Zhang, S. T. Lu, C. Zhang, C. X. Du and H. W. Hou, *CrystEngComm*, 2015, **17**, 846–855; (*b*) F. Habib and M. Murugesu, *Chem. Soc. Rev.*, 2013, **42**, 3278–3288.
41 C. F. Macrae, I. J. Bruno, J. A. Chisholm, P. R. Edgington, P. McCabe, E. Pidcock, L. Rodriguez-Monge, R. Taylor, J. van de Streek and P. A. Wood, *J. Appl. Crystallogr.*, 2008, **41**, 466–470.
42 F. Habib and M. Murugesu, *Chem. Soc. Rev.*, 2013, **42**, 3278–3288.
43 (*a*) *SMART & SAINT software reference manuals, version 6.45*, Bruker Analytical X-ray Systems, Inc., Madison, WI, 2003; (*b*) G. M. Sheldrick, *SADABS, version 2.05, A software for empirical absorption correction*, University of Göttingen, Göttingen, Germany, 2002; (*c*) G. M. Sheldrick, *SHELXTL, version 6.12*, Bruker AXS Inc., Madison, WI, 2001; (*d*) G. M. Sheldrick, *SHELXL97, Program for Crystal Structure Refinement*, University of Göttingen, Göttingen, Germany, 1997; (*e*) G. M. Sheldrick, *Acta Crystallogr., Sect. C: Cryst. Struct. Commun.*, 2015, **71**, 3–8.
44 D. Casanova, M. Llunell, P. Alemany and S. Alvarez, *Chem. – Eur. J.*, 2005, **11**, 1479–1494.
45 J. Xiong, H. Y. Ding, Y. S. Meng, C. Gao, X. J. Zhang, Z. S. Meng, Y. Q. Zhang, W. Shi, B. W. Wang and S. Gao, *Chem. Sci.*, 2017, **8**, 1288–1294.
46 J. K. Tang, I. Hewitt, N. T. Madhu, G. Chastanet, W. Wernsdorfer, C. E. Anson, C. Benelli, R. Sessoli and A. K. Powell, *Angew. Chem., Int. Ed.*, 2006, **45**, 1729–1733.
47 M. Gregson, N. F. Chilton, A. M. Ariciu, F. Tuna, I. F. Crowe, W. Lewis, A. J. Blake, D. Collison, E. J. L. McInnes, R. E. P. Winpenny and S. T. Liddle, *Chem. Sci.*, 2016, **7**, 155–165.
48 K. Katoh, T. Kajiwara, M. Nakano, Y. Nakazawa, W. Wernsdorfer, N. Ishikawa, B. K. Breedlove and M. Yamashita, *Chem. – Eur. J.*, 2011, **17**, 117–122.
49 G. Karlström, R. Lindh, P. Å. Malmqvist, B. O. Roos, U. Ryde, V. Veryazov, P. O. Widmark, M. Cossi, B. Schimmelpfennig, P. Neogrady and L. Seijo, *Comput. Mater. Sci.*, 2003, **28**, 222–239.
50 L. F. Chibotaru, L. Ungur and A. Soncini, *Angew. Chem., Int. Ed.*, 2008, **47**, 4126–4129.
51 L. Ungur, W. Van den Heuvel and L. F. Chibotaru, *New J. Chem.*, 2009, **33**, 1224–1230.
52 L. Ungur, L. F. Chibotaru, C. Aronica, H. Elmoll, G. Pilet and D. Luneau, *J. Am. Chem. Soc.*, 2008, **130**, 12445–12455.
53 S. K. Langley, D. P. Wielechowski, V. Vieru, N. F. Chilton, B. Moubaraki and B. Abrahams, *Angew. Chem., Int. Ed.*, 2013, **52**, 12236–12241.
54 M. E. Lines, *J. Chem. Phys.*, 1971, **55**, 2977–2984.
55 L. F. Zou, L. Zhao, P. Chen, Y. N. Guo, Y. Guo, Y. H. Li and J. K. Tang, *Dalton Trans.*, 2012, **41**, 2966–2971.
56 Q. Chen, J. Li, Y. S. Meng, H. L. Sun, Y. Q. Zhang, J. L. Sun and S. Gao, *Inorg. Chem.*, 2016, **55**, 7980–7987.
57 I. Oyarzabal, J. Ruiz, J. M. Seco, M. Evangelisti, A. Camón, E. Ruiz, D. Aravena and E. Colacio, *Chem. – Eur. J.*, 2014, **20**, 14262–14269.
58 D. Gatteschi, R. Sessoli and L. Sorace, *Handbook on the Physics and Chemistry of Rare Earths*, 2016, vol. 50, pp. 91–139.
59 L. Sun, S. Zhang, C. F. Qiao, S. P. Chen, B. Yin, W. Y. Wang, Q. Wei, G. Xie and S. L. Gao, *Inorg. Chem.*, 2016, **55**, 10587–10596.